A microstructure based yield stress and work-hardening model for textured 6xxx aluminium alloys

M. Khadyko[1,*], O.R. Myhr[1,3], S. Dumoulin[2] and O.S. Hopperstad[1]

[1] *Structural Impact Laboratory (SIMLab), Centre for Research-based Innovation, Department of Structural Engineering, Norwegian University of Science and Technology, NO-7491 Trondheim, Norway*

[2] *SINTEF Materials & Chemistry, NO-7465 Trondheim, Norway*

[3] *Hydro Aluminium, Research and Technology Development (RTD), Romsdalveien 1 NO-6601 Sunndalsøra, Norway*

Abstract

The plastic properties of an aluminium alloy are defined by its microstructure. The most important factors are the presence of alloying elements in form of solid solution and precipitates of various sizes, and the crystallographic texture. A nanoscale model that predicts the work-hardening curves of 6xxx aluminium alloys was proposed by Myhr et al. [1]. The model predicts the solid solution concentration and the particle size distributions of different types of metastable precipitates from the chemical composition and thermal history of the alloy. The yield stress and the work-hardening of the alloy are then determined from dislocation mechanics. The model was largely used for non-textured materials in previous studies. In this work, a crystal plasticity based approach is proposed for the work-hardening part of the nanoscale model, which allows including the influence of the crystallographic texture. The model is evaluated by comparison with experimental data from uniaxial tensile tests on two textured 6xxx alloys in five temper conditions.

Keywords: aluminium alloys; solutes; precipitates; dislocations; work-hardening; crystal plasticity.

[*] Corresponding author: Mikhail Khadyko (mikhail.khadyko@ntnu.no)

1. Introduction

Aluminium alloys are the second most important metallic structural materials after steel and are used in the broadest range of products. The variety of their applications is mirrored by the variety of properties they exhibit. The yield strength, work-hardening and fracture strain of two aluminium alloys may differ by an order of magnitude. Age-hardening may dramatically change these parameters even for the same alloy. In addition some aluminium products, including extruded and rolled sheets, possess considerable plastic anisotropy. Such variety of properties has quite often some common underlying physical mechanisms, which just manifest themselves differently in different conditions. An important task of material science is to uncover these physical mechanisms and to express them through quantitative models, which can be used in practical applications.

The plastic anisotropy was the first characteristic feature of aluminium which was explained by such quantitative physical models. In [2, 3] Taylor developed a theory of plastic deformation of crystals and polycrystals using aluminium for experimental validation. The crystals deform plastically by slip on certain slip systems, defined by crystallographic planes and directions. Therefore the crystalline grains of any metal are intrinsically plastically anisotropic. Polycrystals containing a multitude of grains may be plastically isotropic if the constituent grains are oriented randomly. If some grain orientations are more prominent, or in other words if the polycrystal has a non-random crystallographic texture, the grains with these orientations will have a pronounced contribution to the anisotropy of the whole sample. If the texture of the polycrystal is known, a variety of methods is available to determine the plastic anisotropy, including the full-constraint Taylor model, relaxed-constraint Taylor models, the self-consistent viscoplastic model and finite element models [4-10].

The next aspect of the plastic behaviour of aluminium alloys is their work-hardening. Taylor in [11] and Orowan in [12] introduced the key concept of a dislocation as a defect of the crystal lattice which propagates through the crystal, transfers plastic deformation, carries elastic energy and interacts with other dislocations. Taylor analysed the dislocation structure in the crystal and connected the flow stress in the crystal with its dislocation density. The problem that remained was to determine the evolution of the dislocation density during plastic deformation. Kocks and Mecking [13, 14] proposed an evolution law which consists of two terms. The first term describes the accumulation of dislocations with plastic deformation and is inversely proportional to the mean free path of the dislocation before it is stopped by interaction with another (immobile) dislocation. The second term describes the annihilation of

dislocations during straining (dynamic recovery) and is proportional to the distance between two dislocations with opposite Burgers vectors at which they annihilate each other. Different improvements and modifications have been proposed for this basic model including kinematic hardening [15] and influence of grain size [16, 17]. The original model was formulated with an assumption of homogeneous dislocation density inside the material. Nevertheless, even after a more rigorous analysis, when the dislocation structures inside the grain (dislocation cells) are taken into consideration, the general evolution rule still holds [18, 19].

Aluminium alloys usually contain particles of varying size and chemical composition, such as precipitates, dispersoids and constituent particles. Their interactions with the dislocations and influence on the work-hardening were known for a long time [20, 21]. These interactions were analysed from the point of view of dislocation theory in [22, 23]. It was demonstrated that the dislocation density associated with non-homogeneous plastic deformation around non-shearable particles (geometrically necessary dislocations, as opposed to the statistically stored dislocations) is inversely proportional to the so-called geometric slip distance which in the simplest case (i.e., plate-shaped particles aligned in one direction) is equal to the average distance between the particles. Estrin [24, 25] proposed a generalization of the Kocks-Mecking model where different dislocation accumulation (and consequently work-hardening) mechanisms were represented by their characteristic distances and linearly added together. This approach was used to build models which account for the precipitate particles in [26-28].

The two aspects of aluminium alloys – anisotropy and dislocation density based work-hardening – were combined in a crystal plasticity model in [29] and developed further in [30]. The hardening in this model has the same form as in the Kocks-Mecking model, but acts on each slip system controlling the critical resolved shear stress instead of the global stress. This model only includes the evolution of statistically stored dislocations, but it may be generalized in the same manner as the Kocks-Mecking model with terms for other factors contributing to work-hardening added linearly. These terms will again be inversely proportional to the characteristic distance of the corresponding work-hardening mechanism. A crystal plasticity model which includes grain size influence is developed in [31] while twinning is included by its characteristic distance in [32]. The “characteristic length” approach was extended even to the influence of phase transformations on the work hardening [33]. Nevertheless some critique of the basic assumptions of this approach was published recently [34].

Even if the mechanical properties of an aluminium alloy are closely related with its microstructure, the experimental determination of the microstructure of an alloy is a difficult and tedious task. In [35] and [1] an attempt is made to derive the microstructure from the chemical composition and the thermal history of the alloy. In [1] a complete model for this is proposed, which combines a precipitation model and dislocation based initial yield strength and work-hardening models for the 6xxx family of alloys. It is referred in this article as the Nanostructure Model (NaMo). The theory behind the model is developed by Myhr and co-workers in [36-38]. The work-hardening model is a version of the Kocks-Mecking equation formulated in terms of global stress and strain. In [39], the NaMo precipitation model was used together with a crystal plasticity model to study the influence of precipitates on the work-hardening and anisotropy of the aluminium alloys. The crystal plasticity model was of the Kocks-Mecking type, similar to the model in the present work, with two main differences being the precipitate particle description and the latent hardening description. The precipitates were assumed to be rod-shaped (in contrast to the NaMo assumption of spherical precipitate shape) and their influence on the stress-strain response and plastic anisotropy was calculated using the Eshelby equations for the elastic inclusion in an elastoplastic medium. The model was used only for moderate strains, assuming unbounded growth of the geometrically necessary dislocation density. This approach was utilized primarily to study the influence of such precipitates on the plastic behaviour of a single crystal. The experimental part included uniaxial tensile tests applied to an alloy with negligible texture with various heat treatments.

NaMo, as formulated in [1], is treating the polycrystalline nature of aluminium in a very simplified manner, reducing the texture and grain rotation effects to one constant parameter. Furthermore, it was calibrated and tested on aluminium alloys with random texture. In the present work, the effects of crystallographic texture are implemented into NaMo more properly using the crystal plasticity theory. Thus, the effects of plastic anisotropy, due to crystallographic texture and its evolution, on the initial yield stress and work-hardening are included in the model. For this purpose a work-hardening model is proposed for crystal plasticity, which includes the effect of solid solution and precipitate particles on the slip system level. The information about the solid solution concentration and the precipitate particles comes directly from the precipitation model of NaMo. The results from two series of tensile tests have been reported previously by Khadyko et al. for different temper conditions of the AA6060 and AA6082 alloys with pronounced texture [40] and for different material directions of the AA6060 alloy [41]. In the current paper, these

experimental results were compared to the predictions of NaMo with and without the crystal plasticity modification. The tests for different alloys and tempers allow evaluating the capability of the precipitation model of NaMo for textured aluminium alloys and to which extent the deviations between predictions and experimental data are caused by crystallographic texture effects. The tests for different material directions allow evaluating the capability of the crystal plasticity part in describing the alloy's plastic anisotropy and to better evaluate the role of texture evolution on the work-hardening.

2. Experiments

The two series of quasi-static tensile tests on cylindrical specimens of aluminium alloys AA6060 and AA6082, previously reported by Khadyko et al. [40, 41], are briefly recapitulated in the following for completeness. The compositions of the two alloys are given in Table 1. The specimens were taken from 10 mm thick and 90 mm wide extruded flat profiles at 90° to the extrusion direction and were given a separate solution heat treatment at 540^{o} C for 15 minutes before they were quenched to room temperature and subsequently aged to tempers T4, T6x, T6, T7 and O, where the T4 temper corresponds to one week room temperature storage. The heat treatment is described in more detail in Table 2. The AA6060 alloy in T4 temper was also used for the tensile tests in different material directions. The cylindrical specimens were cut from the profile at different angles θ to the extrusion direction with 22.5° interval (i.e., θ equals 0°, 22.5°, 45°, 67.5° and 90°). To represent the anisotropic properties of the material, a rectangular coordinate system xyz is defined such that the x-axis is in the transverse direction, the y-axis is in the longitudinal direction of the specimen, and the z-axis is always in the thickness direction of the extruded profile.

The uniaxial tensile tests were performed in a testing machine with laser gauges, allowing precise measurements of the specimen's minimum diameter at high frequency. The test set-up made it possible to obtain the true stress-strain curve until fracture for all specimens. The crystallographic texture of the alloys was measured with a scanning electron microscope using electron back-scattering diffraction (EBSD). The EBSD measurements were carried out in the plane defined by the extrusion and normal directions of the profile, using 10 µm steps on a square grid for the AA6060 alloy and 5 µm steps for the AA6082 alloy. The ODFs presented in Figure 1 were calculated from the pole figures in the EDAX TSL OIM software using a harmonic series expansion and triclinic sample symmetry [42]. The textures are

typical for recrystallized alloys (AA6060) and non-recrystallized extruded alloys (AA6082), respectively. The most prominent texture component in both alloys is a cube component, but the other orientations differ strongly between AA6060 and AA6082. The texture of the AA6060 alloy is comprised of a strong cube texture with a minor Goss component, while the AA6082 alloy has a cube texture with orientations along the β-fibre, which runs from the Copper to the Brass orientation, through the S component.

The true stress–strain curves obtained in the tensile tests include the contribution of the triaxial stress field, arising in the neck after localization. To remove the triaxial field contribution and obtain the equivalent stress-strain curve for the material the following procedure was used. A finite element model of the tensile specimen was built, with the material described by an anisotropic plasticity model using a two-term Voce work-hardening rule. The tensile test was simulated and the true stress-strain curve from the simulation was fitted to the true stress-strain curve from the experiments by optimizing the parameters of the two-term Voce work-hardening rule. Thus the equivalent stress-strain curve until fracture was obtained for each material, see [40] for a more complete description of the procedure. It should be noted that the equivalent stress-strain curves were determined by using the extrusion direction as the reference direction; i.e., the obtained equivalent stress-strain curves are consistent with true stress vs. logarithmic plastic strain curves from uniaxial tension tests in the extrusion direction. The test specimens on the other hand were cut at 90° to the extrusion direction, because the results from tension tests in the in-plane transverse direction tend to be more consistent and reliable. The results are presented in Figure 2. Henceforth the equivalent stress or the flow stress in uniaxial tension (without the additional triaxial field caused by necking) is denoted as σ. For the specimens cut in material direction θ this flow stress is denoted as σ_θ and found using the Bridgman correction [43] as formulated in [44]:

$$\sigma_\theta = \frac{\sigma_y}{\left(1+2R/\bar{a}\right)\cdot \ln\left(1+\bar{a}/2R\right)} \qquad (0)$$

where σ_y is the true stress, $\bar{a}$ is the minimum radius and R is the radius of curvature of the neck. The geometry of the neck was estimated by the relation

$$\frac{\bar{a}}{R} = k\left(\varepsilon_\theta^p - \varepsilon_{\theta u}^p\right) \qquad (0)$$

where $\varepsilon_{\theta u}^{p}$ is the logarithmic plastic strain at the start of necking at orientation θ and k is a parameter. This parameter was found for the 90° direction by fitting the corrected stress-strain curve found from Equation (1) to the equivalent stress-strain curve found from the optimization procedure described above. The obtained value of $k = 0.9$ was then used for all other orientations, while $\varepsilon_{\theta u}^{p}$ was found directly from the directional tensile tests, see [41] for a more detailed account of the procedure.

3. Theoretical foundation

3.1. Nanostructure model (NaMo).

A detailed outline of the theory and assumptions lying in the foundation of NaMo is given elsewhere [1, 36-38], therefore only a review of the key ideas and equations will be given here. The model consists of three parts: a precipitation model, a yield strength model and a work-hardening model.

3.1.1. Precipitation model

The chemical composition of the alloy and the thermal history are used as an input for the precipitation model. Time is discretized into small steps. The first component of the model is the nucleation law. It predicts the number of stable nuclei, which form at every time step. The incubation period is neglected and the steady state nucleation rate j calculated according to

$$j = j_0 \exp\left[-\left(\frac{A_0}{\mathrm{R}T}\right)^3 \left(\frac{1}{\ln\left(\bar{C}/C_e\right)}\right)^2\right] \exp\left(-\frac{Q_d}{\mathrm{R}T}\right) \tag{0}$$

where the first exponential term expresses the energy barrier against heterogeneous nucleation, and the second accounts for the temperature dependency of the diffusion coefficient. Further, T is the temperature, R is the universal gas constant, $\bar{C}$ is the mean solute concentration in the matrix, C_e is the equilibrium solute concentration at the particle/matrix interface, A_0 is a parameter related to the energy barrier for nucleation, Q_d is the activation energy for diffusion and j_0 is a pre-exponential term. The nucleated particles are idealized as spherical and are characterized by their radius r, solute concentration C_p and

an interface energy. These particles may either dissolve or grow as described by the second component of the model – the particle radius rate law

$$\frac{dr}{dt} = \frac{\bar{C} - C_i}{C_p - C_i} \frac{D}{r} \tag{0}$$

where C_i is the solute concentration at the particle/matrix interface and D is the temperature dependent diffusion coefficient. The Gibbs-Thomson equation [36] is used to relate C_i to the equilibrium concentration C_e. When this equation is combined with Equation (4), an expression for the critical radius r_0 for a particle that neither dissolves nor grows can be derived. At a certain time step during a heat treatment, particles smaller than r_0 dissolve while particles larger than r_0 grow, which leads to the evolution of a distribution of particles of various size, i.e., a discrete particle size distribution (PSD) with a defined number of particles within each size class $r \pm (\Delta r / 2)$ (if $\Delta r \to 0$ then the function becomes continuous).

A range of different particles may form in 6xxx alloys depending on the chemical composition and the heat treatment, but the ones that are of main interest here are the nanometre scale hardening particles consisting of Mg and Si (e.g. β'' and β' particles), as well as clusters and GP-zones, which may form at room temperature. Each of these classes or groups of particles is represented by a separate PSD in the model, i.e., one PSD for β'' and β' particles and one for clusters and GP-zones. Since the model assumes that the metastable phases consist of Mg and Si, precipitates containing other elements, such as the Cu-containing Q-phase, are not accounted for. The variation in precipitate size that can be handled by the model ranges from less than 1nm to about 100nm with respect to the equivalent spherical radius, and NaMo has been shown to give reasonable predictions of number density and average size for precipitates within this span in magnitude (see e.g. [37] and [38]).

The third component of the model is the continuity equation. It is used to find the mean solute concentration $\bar{C}$ in the matrix, and is based on the fact that even though there may be a transition between elements in solid solution and in the particles comprising the two PSDs during a heat treatment, the overall content of each alloying element remains constant. The continuity equation reads [45]

$$\bar{C} = \frac{C_0 - \left(C_{p1} \sum_i \frac{4}{3}\pi r_i^3 N_i + C_{p2} \sum_j \frac{4}{3}\pi r_j^3 N_j \right)}{1 - \left(\sum_i \frac{4}{3}\pi r_i^3 N_i + \sum_j \frac{4}{3}\pi r_j^3 N_j \right)} \quad (0)$$

where C_0 is the initial solute concentration in the alloy, C_{p1} and C_{p2} are the concentration of alloying element in particles which belong to each of the two size distributions. N_i and N_j are the number of particles per unit volume within the discrete radius intervals $r_i \pm (\Delta r / 2)$ and $r_j \pm (\Delta r / 2)$ corresponding to each of the distributions.

3.1.2. Yield strength model

The yield strength model uses dislocation theory to convert the results from the precipitation model, i.e., the mean solute concentration and the PSD, into a corresponding room temperature yield stress. It considers two kinds of contributions: precipitation strengthening σ_p and solid solution strengthening σ_{ss}, in addition to the intrinsic strength of the pure aluminium σ_i.

The precipitation strengthening contribution σ_p corresponds to the difference in yield stress between a material containing particles and an identical material without particles. For the former material, σ_p can be attributed to the extra stress needed for a dislocation to break away from particles acting as obstacles along the dislocation line when the dislocation starts to move. A reasonable expression for σ_p can be obtained by calculating the mean obstacle strength of particles that interact with a bowing dislocation along the entire dislocation line by considering the specific strength of each individual particle according to the two governing mechanisms, i.e., shearing of smaller particles and Orowan bypassing of larger particles that exceed a critical radius. In addition, the mean effective particle spacing must be calculated from the particle size distribution using the Friedel formalism [46] before σ_p can be obtained as described in [47].

The solid solution contribution is due to individual atoms of Si, Mg, Mn and Cu that are present in the aluminium matrix. These atoms serve as weak obstacles for the dislocations and their overall strength contribution is calculated using the framework outlined in [37, 46]. When several strengthening mechanisms are operating simultaneously, it is assumed that their

contributions may be added linearly. Thus the total initial yield strength of the material is calculated as

$$\sigma_y = \sigma_i + \sigma_{ss} + \sigma_p \tag{0}$$

3.1.3. Work-hardening model

The work-hardening model is based on the assumption that the total dislocation density may be decomposed into two parts: the statistically stored and geometrically necessary dislocation densities ρ_s and ρ_g, respectively, which evolve independently from each other. These two contributions to the dislocation density may be added linearly and applied in the Taylor equation to obtain the work-hardening as [11]

$$\Delta\sigma_d \equiv \sigma - \sigma_y = \alpha M \mu b \sqrt{\rho_s + \rho_g} \tag{0}$$

where α is a constant, M is the Taylor factor, μ is the shear modulus and b is the magnitude of the Burgers vector. The evolution of ρ_s is described by the Kocks-Mecking equation [14]

$$d\rho_s = \left(k_1\sqrt{\rho_s} - k_2\rho_s\right)d\varepsilon^p \tag{0}$$

where k_1 characterizes the generation of dislocations and is assumed constant for the 6xxx family of alloys, k_2 is the recovery term which depends on the solid solution concentration and ε^p is the equivalent plastic strain. This expression may be integrated analytically which gives

$$\rho_s = \left(\frac{k_1}{k_2}\right)^2 \left(1 - \exp\left(-\frac{k_2\varepsilon^p}{2}\right)\right)^2 \tag{0}$$

The dependence of k_2 on the concentration of elements in solid solution arises from several mechanisms [13, 14] related to the ease of dislocations of opposite sign to annihilate by glide and cross-slip and is described by

$$k_2 = k_1 \frac{\alpha M \mu b}{k_3 \left(\hat{C}_{Mg}\right)^{3/4}} \tag{0}$$

Here k_3 is a parameter, determined by calibration against experimental data, and $\hat{C}_{Mg}$ is the equivalent magnesium concentration, which is a parameter that accounts for the contribution

of different alloying elements to dynamic recovery. For 6xxx alloys, a reasonable estimate is the following [1]: $\hat{C}_{Mg} = \overline{C} + 0.5C_{Si}^{eff}$, where C_{Si}^{eff} is the effective silicon concentration, which is obtained through a correction for the amount of Si being tied up as coarse particles [37]. It is noted that $\overline{C}$ is taken as the mean concentration of Mg in solid solution for 6xxx alloys.

The evolution of the geometrically necessary dislocation density is a variation of the Ashby equation [23], adapted for the global plastic strain

$$\rho_g = \frac{k_4}{b\lambda_{g,o}}\varepsilon^p \tag{0}$$

where k_4 is a parameter, determined by calibration to tests and $\lambda_{g,o}$ is the characteristic geometric slip distance associated with the Orowan particles. The geometrically necessary dislocation density only increases up to a certain value, at which recovery mechanisms are triggered (i.e., decohesion or fracture of the particles or nucleation of new dislocations at the particle/matrix interface [1]), and which prevent a further accumulation of dislocations. The critical plastic strain ε_c at which this occurs depends on the volume fraction of the Orowan particles f_o, namely

$$\varepsilon_c = \left(\frac{f_o^{ref}}{f_o}\right)\varepsilon_c^{ref} \tag{0}$$

where f_o^{ref} and ε_c^{ref} are the corresponding values of a reference alloy. The precipitation model provides information about both the geometric slip distance $\lambda_{g,o}$ and the volume fraction of the Orowan particles f_o [45], i.e.,

$$\lambda_{g,o} = \left(8\sum_i r_i^2 N_i\right)^{-1} \quad \text{for } r_i > r_c \tag{0}$$

$$f_o = \sum_i \frac{4}{3}\pi r_i^3 N_i \quad \text{for } r_i > r_c \tag{0}$$

where r_c is the particle radius defining the transition between shearable and non-shearable particles. Note that $\lambda_{g,o}$ and f_o are calculated from just one of the two PSDs, i.e., the PSD

representing β'' and β' particles, since for the other distribution representing clusters and GP-zones, all particles are less than the critical radius (i.e., $r_i < r_c$).

3.2. Crystal plasticity model

3.2.1. Single crystal kinematics and kinetics

The finite deformation formulation of single crystal plasticity is used. The deformation gradient $\boldsymbol{F}$ is multiplicatively decomposed into an elastic part $\boldsymbol{F}^e$ and a plastic part $\boldsymbol{F}^p$ as

$$\boldsymbol{F} = \boldsymbol{F}^e \boldsymbol{F}^p \tag{0}$$

Here $\boldsymbol{F}^p$ accounts for plastic slip and transforms the crystal from the initial configuration Ω_0 into the intermediate plastically deformed configuration $\bar{\Omega}$, while $\boldsymbol{F}^e$ accounts for the elastic deformations and rigid body rotations and transforms the crystal from the intermediate configuration $\bar{\Omega}$ into the current configuration Ω. The slip systems are defined by the slip direction vector $\boldsymbol{m}_0^\alpha$ and the slip plane normal vector $\boldsymbol{n}_0^\alpha$ in the initial configuration. They stay the same in the intermediate configuration and transform into vectors $\boldsymbol{m}^\alpha$ and $\boldsymbol{n}^\alpha$, respectively, in the current configuration. These vectors may be used as a basis of the plastic velocity gradient $\bar{\boldsymbol{L}}^p$ in the intermediate configuration

$$\bar{\boldsymbol{L}}^p = \dot{\boldsymbol{F}}^p \left(\boldsymbol{F}^p\right)^{-1} = \sum_{\alpha=1}^{n} \dot{\gamma}^\alpha \boldsymbol{m}_0^\alpha \otimes \boldsymbol{n}_0^\alpha \tag{0}$$

where $\dot{\gamma}^\alpha$ is the slip rate on slip system α in the intermediate configuration and n is the total number of slip systems.

The elastic Green strain tensor $\bar{\boldsymbol{E}}^e$ with respect to the intermediate configuration may be defined as

$$\bar{\boldsymbol{E}}^e = \frac{1}{2}\left[\left(\boldsymbol{F}^e\right)^T \boldsymbol{F}^e - \boldsymbol{I}\right] = \frac{1}{2}\left(\bar{\boldsymbol{C}}^e - \boldsymbol{I}\right), \quad \bar{\boldsymbol{C}}^e = \left(\boldsymbol{F}^e\right)^T \boldsymbol{F}^e \tag{0}$$

where $\bar{\boldsymbol{C}}^e$ is the elastic right Cauchy-Green deformation tensor and $\boldsymbol{I}$ is the second-order unity tensor. If the Cauchy stress tensor $\boldsymbol{\sigma}$ is pulled back into the intermediate configuration, the second Piola-Kirchhoff stress tensor $\bar{\boldsymbol{S}}$ is obtained

$$\bar{\boldsymbol{S}} = \det\boldsymbol{F}\left(\boldsymbol{F}^e\right)^{-1}\boldsymbol{\sigma}\left(\boldsymbol{F}^e\right)^{-T} \tag{0}$$

By assuming small elastic deformations, it is reasonable to adopt a linear hyperelastic model to describe the elastic behaviour

$$\bar{\boldsymbol{S}} = \mathbf{C}_{el}^{\bar{S}} : \bar{\boldsymbol{E}}^e \tag{0}$$

where $\mathbf{C}_{el}^{\bar{S}}$ is the fourth-order tensor of elastic moduli.

The total power per unit volume $\dot{w}$ consists of elastic and plastic parts

$$\dot{w} = \dot{w}^e + \dot{w}^p = \bar{\boldsymbol{S}} : \dot{\bar{\boldsymbol{E}}}^e + \bar{\boldsymbol{C}}^e\bar{\boldsymbol{S}} : \bar{\boldsymbol{L}}^p \tag{0}$$

The plastic power may be rewritten as a sum of powers spent on all the slip systems

$$\dot{w}^p = \sum_{\alpha=1}^{n} \tau^\alpha \dot{\gamma}^\alpha \tag{0}$$

where τ^α is the resolved shear stress on slip system α, power conjugate to the slip rate $\dot{\gamma}^\alpha$, and may be found from the second Piola-Kirchhoff stress tensor as

$$\tau^\alpha = \bar{\boldsymbol{C}}^e\bar{\boldsymbol{S}} : \left(\boldsymbol{m}_0^\alpha \otimes \boldsymbol{n}_0^\alpha\right) \tag{0}$$

3.2.2. Flow and work-hardening rules

The plastic flow is described by a rate-dependent rule

$$\dot{\gamma}^\alpha = \dot{\gamma}_0 \left(\frac{\left|\tau^\alpha\right|}{\tau_c^\alpha}\right)^{\frac{1}{m}} \operatorname{sgn}\left(\tau^\alpha\right) \tag{0}$$

where $\dot{\gamma}_0$ is the reference slip rate, m is the instantaneous strain rate sensitivity and τ_c^α is the history dependent critical resolved shear stress of slip system α. The initial value of yield strength is equal to $\tau_c^\alpha = \tau_y$ for all slip systems.

We introduce work-hardening by connecting the critical resolved shear stress rate $\dot{\tau}_c^\alpha$ to the slip rates on the slip systems

$$\dot{\tau}_c^{\alpha} = \theta \sum_{\beta=1}^{n} q_{\alpha\beta} \left| \dot{\gamma}^{\beta} \right| \tag{0}$$

where $\theta \equiv d\tau_c / d\Gamma$ is the hardening rate defined by a master curve, and $q_{\alpha\beta}$ is the matrix of self-hardening and latent-hardening coefficients. The accumulated slip Γ is defined by the evolution equation

$$\dot{\Gamma} = \sum_{\alpha=1}^{n} \left| \dot{\gamma}^{\alpha} \right| \tag{0}$$

The master hardening curve is given by

$$\tau_c = \tau_y + \alpha \mu b \sqrt{\rho_s + \rho_g} \tag{0}$$

where ρ_s and ρ_g are the average densities of statistically stored and geometrically necessary dislocations, respectively. Similarly to NaMo, it is assumed that the two dislocation densities may be added linearly and used in the Taylor equation to obtain the work-hardening. The dislocation density evolutions are connected to the accumulated slip by

$$d\rho_s = \left(k_1^{cp} \sqrt{\rho_s} - k_2^{cp} \rho_s \right) d\Gamma \tag{0}$$

$$d\rho_g = \frac{1}{bL} \left(1 - \left(\frac{\rho_g}{\rho_g^{sat}} \right)^a \right) d\Gamma \tag{0}$$

where k_1^{cp} and k_2^{cp} are in turn the accumulation and annihilation terms for statistically stored dislocations, L is a parameter proportional to the characteristic distance between the Orowan particles, and ρ_g^{sat} is the density of geometrically necessary dislocations at saturation. The evolution of the geometrically necessary dislocation density is formulated in a slightly different manner than in NaMo, while keeping the behaviour of linear increase and fast saturation at some critical value. The value of parameter a may be chosen high enough to approach Equation (11) as closely as necessary. Here $a = 10$ is used. The work-hardening rate θ is the derivative of the master curve τ_c with respect to the accumulated slip Γ, viz.

$$\theta \equiv \frac{d\tau_c}{d\Gamma} = \frac{\partial \tau_c}{\partial \rho_s} \frac{d\rho_s}{d\Gamma} + \frac{\partial \tau_c}{\partial \rho_g} \frac{d\rho_g}{d\Gamma} \tag{0}$$

which by use of Equations (27) and (28) may be rewritten as

$$\theta = \frac{\alpha\mu b}{2\sqrt{\rho_s + \rho_g}}\left(k_1^{cp}\sqrt{\rho_s} - k_2^{cp}\rho_s + \frac{1}{bL}\left(1 - \left(\frac{\rho_g}{\rho_g^{sat}}\right)^a\right)\right) \tag{0}$$

3.2.3. Polycrystal modelling

The behaviour of the polycrystal is modelled using the assumption of a constant deformation gradient in all grains – i.e., the full-constraint Taylor model. This model does not provide stress equilibrium between the grains and usually slightly overestimates the global stress. Nevertheless, it is still fairly accurate and computationally efficient. The use of this model for predicting the yield stress anisotropy against other models (relaxed constraint, self-consistent and finite element models) is discussed in [4] and [48].

The deformation gradient is equal to the global deformation gradient for all constituent grains and the global Cauchy stress $\boldsymbol{\sigma}$ is found as an average of the local Cauchy stresses $\boldsymbol{\sigma}_k$ in the grains

$$\boldsymbol{\sigma} = \frac{1}{n_g}\sum_{k=1}^{n_g}\boldsymbol{\sigma}_k \tag{0}$$

where n_g is the number of grains. The contribution of all grains to the total stress is the same, meaning it is assumed they all have equal volume.

The plastic rate-of-deformation tensor $\bar{\boldsymbol{D}}_k^p$ for grain k may be defined as the symmetric part of $\bar{\boldsymbol{L}}_k^p$, i.e.,

$$\bar{\boldsymbol{D}}_k^p = \frac{1}{2}\left(\bar{\boldsymbol{L}}_k^p + \left(\bar{\boldsymbol{L}}_k^p\right)^T\right) \tag{0}$$

and is used to express the equivalent plastic strain rate in grain k by

$$\dot{\varepsilon}_k^p = \sqrt{\frac{2}{3}\bar{\boldsymbol{D}}_k^p : \bar{\boldsymbol{D}}_k^p} \tag{0}$$

The Taylor factor M of the polycrystal is then defined as the ratio of the average slip rate to the average equivalent plastic strain rate over all the grains, i.e.,

$$M = \frac{\frac{1}{n_g}\sum_{k=1}^{n_g}\dot{\Gamma}_k}{\frac{1}{n_g}\sum_{k=1}^{n_g}\dot{\varepsilon}_k^p} \tag{0}$$

where it was used that all grains are assumed to have equal volume in the full-constraint Taylor model.

4. Parameter identification

Before NaMo may be used to calculate the stress-strain curve of a 6xxx aluminium alloy, it must be calibrated against experimental data. The parameters that need to be calibrated are:

- the dislocation accumulation coefficient, k_1
- the coefficient connecting the equivalent Mg concentration and the dynamic recovery, k_3
- the coefficient connecting the characteristic slip distance and the geometrically necessary dislocation accumulation, k_4
- the reference critical strain, ε_c^{ref}
- the reference particle volume fraction, f_o^{ref}

The parameters k_1 and k_2 are found by fitting Equation (8) for work-hardening and Equation (9) for statistically stored dislocation density to the experimental stress-strain curves for two specimens made from different alloys, but heat-treated to the same temper, for which there is no considerable particle influence (in this case W10 temper, see [1] for more details); k_3 is then found from the obtained k_2. The remaining parameters k_4, ε_c^{ref} and f_o^{ref} are found by fitting the same equations and in addition Equation (11) for the geometrically necessary dislocation density to the experimental stress-strain curve of a specimen which is heat treated to a temper with considerable influence of precipitate particles on the response (namely T7 temper). The details of the calibration and the parameter values for 6xxx alloys may be found in [1]. It should be noted here that NaMo was calibrated for 6xxx alloys in [1] using a different set of experimental data than the one used in this work. The calibrated NaMo was

then used to predict the behaviour of the AA6060 and AA6082 alloys based only on their chemical composition and thermal history, without any further calibrations.

To use the crystal plasticity version of the hardening model (CP-NaMo), it is necessary to find out how the output of the precipitation model of NaMo is connected to the parameters of CP-NaMo. The accumulation coefficient k_1^{cp} is assumed constant for the 6xxx family of alloys, in the same way as k_1. The dynamic recovery coefficient k_2^{cp} is assumed to depend on the equivalent magnesium concentration in the same form as k_2, i.e.,

$$k_2^{cp} = k_1^{cp} \frac{\alpha \mu b}{k_3^{cp} \left(\hat{C}_{Mg} \right)^{3/4}} \tag{0}$$

where k_3^{cp} is a parameter. The parameter L is proportional to the slip distance $\lambda_{g,o}$, viz.

$$L = k_4^{cp} \lambda_{g,o} \tag{0}$$

where k_4^{cp} is a parameter. It should be noted that $\lambda_{g,o}$ is calculated from the precipitation model and has a direct physical meaning of slip distance, while L is a parameter proportional to it, but also including the contribution of the calibration procedure. The geometrically necessary dislocation density increases until the saturation value ρ_g^{sat} is reached, which happens when the accumulated slip reaches its critical value Γ_c. This value in turn depends on the volume fraction of Orowan particles f_o analogously to Equation (12), i.e.,

$$\Gamma_c = \left(\frac{f_o^{ref}}{f_o} \right) \Gamma_c^{ref} \tag{0}$$

Provided that parameter a in Equation (28) is sufficiently large, the saturation value of the geometrically necessary dislocation density may be estimated without much loss of accuracy as

$$\rho_g^{sat} \approx \frac{\Gamma_c}{bL} = \frac{k_5^{cp}}{f_o bL} \tag{0}$$

where k_5^{cp} is a parameter, which includes the reference values of the particle volume fraction f_o^{ref} and the critical accumulated slip Γ_c^{ref}.

In summary, the set of constants, which must be determined for CP-NaMo, is the following

- the dislocation accumulation coefficient, k_1^{cp}
- the coefficient connecting the equivalent Mg concentration and the dynamic recovery, k_3^{cp}
- the coefficient connecting the slip distance and the geometrically necessary dislocation accumulation, k_4^{cp}
- the coefficient defining the saturation density of the geometrically necessary dislocations, k_5^{cp}

The initial slip resistance τ_y is found directly from NaMo's yield stress model. NaMo uses the stress relations formulated on slip system level and multiplies the resulting stresses by the Taylor factor to transform them to global stresses. If this multiplication is left out, we obtain

$$\tau_y = \tau_i + \tau_p + \tau_{ss} \tag{0}$$

where the contribution to the yield stress from the intrinsic strength of aluminium, the particles and the solid solution are denoted τ_i, τ_p and τ_{ss}, respectively.

The numerical set up of CP-NaMo consists of an 8-node element with reduced integration (i.e., only a single integration point), using full-constraint Taylor type homogenization in the integration point. The explicit solver of the nonlinear finite element program LS-DYNA was used. The crystal plasticity material model is implemented as a user material subroutine. This subroutine utilizes the explicit integration scheme presented by Grujicic and Batchu [49]. The single integration point, full-constraint Taylor method may seem rather crude, but in stress calculations in uniaxial tension it demonstrates quite accurate results, comparable to much more computationally heavy finite element models of the polycrystals (CP-FEM). When the tensile tests in different material directions were modelled, the crystallographic texture utilised in the simulations was rotated by an appropriate angle around the *z*-axis.

The goal of the calibration was to find a set of parameters k_i^{cp} that would result in the same stress-strain response from CP-NaMo and NaMo for the reference materials. The first two reference materials are AA6060 and AA6082 in T4 temper with random texture. They were chosen because the geometric slip distance for these materials is very high, meaning that

their stress-strain response is not influenced by the precipitates. Therefore, the k_1^{cp} and k_2^{cp} coefficients may be isolated and used to find the coefficient k_3^{cp}. The stress-strain curves of the reference materials were found using NaMo. The CP-NaMo response was then fitted to them with LS-OPT [50]. LS-OPT is an optimization program that runs several LS-DYNA simulations with different values of material parameters and compares the results of the simulations with some reference data. The mean squared error is calculated for each set of values and new values are chosen in such a way that the mean squared error is reduced. Usually after 15-20 iterations an optimal set of values is found. This procedure was used for the two aforementioned materials, utilizing the same k_1^{cp} and two different k_2^{cp} as the parameters varied by LS-OPT. When the two k_2^{cp} were found, they were used in Equation (35) , together with the equivalent Mg concentration, known from the precipitation model, to find k_3^{cp}.

The second step was to find the precipitate related constants. For this the AA6060 alloy with random texture in T6 temper was chosen. The geometrical slip distance for this material was small enough to show a considerable influence on the stress-strain response. The coefficient k_2^{cp} for this alloy follows from the already determined coefficient k_3^{cp}, whereas k_1^{cp} is the same for all alloys. The parameters L and ρ_g^{sat} (and thereby k_4^{cp} and k_5^{cp}), were found by adjusting them in such a way that ρ_g would grow at the same rate and saturate at the same value compared to ρ_s in CP-NaMo as in NaMo, i.e.

$$\left(\frac{\rho_g^{sat}}{\rho_s^{sat}}\right)_{\text{CP-NaMo}} = \left(\frac{\rho_g^{sat}}{\rho_s^{sat}}\right)_{\text{NaMo}} \tag{0}$$

and

$$\left(\frac{\Gamma_g^{sat}}{\Gamma_s^{sat}}\right)_{\text{CP-NaMo}} = \left(\frac{\varepsilon_g^{sat}}{\varepsilon_s^{sat}}\right)_{\text{NaMo}} \tag{0}$$

where ε_g^{sat} and ε_s^{sat} are plastic strain values at which geometrically necessary and statistically stored dislocation densities saturate in NaMo, while Γ_g^{sat} and Γ_s^{sat} are the analogous accumulated slip values in CP-NaMo. The principle is illustrated in Figure 3, where the

dislocation densities ρ_s and ρ_g for NaMo and CP-NaMo are plotted as functions of plastic strain ε^p. The values for CP-NaMo are taken from a simulation of a single crystal with Euler angles $\varphi_1 = 0°$, $\Phi = 0°$ and $\varphi_2 = 0°$ (i.e., the cube orientation). The slopes and saturation values of these curves are therefore not equal for NaMo and CP-NaMo on this plot, but they are proportional for the geometrically necessary and statistically stored dislocation densities. One may also notice the sharp corner on the ρ_g - ε^p curve for NaMo, where it switches to a constant value upon saturation, while for CP-NaMo the transition is smooth. Notice that the initial value of ρ_s and ρ_g is a non-zero positive number, which is negligible compared to the average level of dislocation densities during the deformation. In case of T4, O and T6x the parameters associated with the precipitate particles (characteristic distance and saturation density) have some extreme values, which just indicate that the precipitates do not play any role in their response by the Orowan looping mechanism.

The remaining of crystal plasticity model parameters were taken from literature (e.g. [7]). Their values are shown in Table 3.

The stress-strain curves from NaMo and CP-NaMo are presented in Figure 4. Because NaMo uses the Taylor factor $M = 3.1$ corresponding to random texture, a set of 1000 random orientations was used as the input into the calculations. In NaMo this value stays the same throughout the deformation, but in CP-NaMo it evolves, as may be seen in Figure 5. The difference in Taylor factor is as high as 15% for large strains, leading to different shape of the stress-strain curve. NaMo has a characteristic saturation of the stress, where the hardening rate falls practically to zero, while CP-NaMo for random texture continues to harden even when the dislocation densities on active slip systems have saturated, because of the evolution of the Taylor factor. Another difference is the latent hardening parameter $q_{\alpha\beta}$ in CP-NaMo, which is not found in NaMo and could hardly be implemented in it in a simple way. So, if this is taken into account, obtaining exactly the same stress-strain curves with CP-NaMo and NaMo is not possible (and probably not desired) in some cases. The data from the precipitation model, used as the input, is given in Table 4 and the obtained parameters of CP-NaMo are given in Table 5. The physical meaning of the extreme values of L and ρ_g^{sat} for the T4, T6x and O tempers is just that for these tempers the production of geometrically necessary dislocation is effectively non-existent and the precipitates do not contribute to the work-hardening. The

coefficient k_1^{cp}, constant for all materials (i.e., combinations of alloy and temper), is equal to $1.25 \cdot 10^5 \text{ mm}^{-1}$.

We attempted a more direct calibration, where the experimental curves and CP-NaMo were used from the very beginning, but this attempt failed. Notably, the stress-strain curves in temper T4 for the two alloys did not fall into the assumed framework in which the work-hardening is controlled solely by the equivalent Mg concentration, and the obtained values of k_2^{cp} did not allow to find a reasonable value of k_3^{cp}.

5. Results

Using the parameters determined in Section 4 and the measured crystallographic texture, CP-NaMo was applied in combination with the full-constraint Taylor model to compute the equivalent stress-strain curves of all the tested alloy/temper combinations and these curves were compared to those obtained experimentally and with NaMo. In this procedure, the crystallographic texture of the alloy was used. NaMo is formulated in terms of slips and resolved shear stresses, and uses the Taylor factor $M = 3.1$ to find the global stress and strain. This approach is reasonable to use for alloys exhibiting random texture (and perhaps weak texture), but in the case of the present experiments the texture is not random. Instead of a constant Taylor factor, we obtain a value relevant for the actual alloy and also its possible evolution, as shown in Section 4. The equivalent stress-strain curves obtained from NaMo and CP-NaMo are compared with the experimental curves for all alloy/temper combinations in Figure 6.

In the case of the AA6060 alloy, the stress-strain curves of the tempers with high precipitate contents (i.e., tempers T6 and T7) are predicted reasonably well by NaMo, even in the quantitative sense. The stress level is slightly overestimated for temper T6 and underestimated for temper T7. The predictions for temper T4 are less accurate, mainly because the work-hardening rate decreases too rapidly and the stress saturates at a lower value than in the experiment. The predictions for the T6x and O tempers are the least accurate. The O temper has the lowest stress levels of all tempers in the experiment, while NaMo predicts a stress level similar to temper T4. The yield stress and saturation stress of the T6x temper are overestimated, while the work-hardening rate drops to almost zero much faster than in the experiment. With respect to the texture of the AA6060 alloy, the actual Taylor factor is considerably lower than for a random texture, as seen in Figure 5. Consequently, the

predictions with CP-NaMo show the same pattern as the predictions with NaMo, but CP-NaMo predicts lower stress levels due to the lower Taylor factor. With the exception of the T7 temper, the predictions exhibit too rapid decrease of the work-hardening rate and consequently premature saturation of stress to a constant value. The evolving Taylor factor in the CP-NaMo calculations compensate for this but only slightly (the evolution of Taylor factor for AA6060 is insignificant) and not even closely to a sufficient degree. Another difference between the model predictions may be seen e.g. for tempers T6 and T7. The work-hardening rate predicted by NaMo drops very abruptly when the geometrically necessary dislocations stop to accumulate. This behaviour is not observed in the experiments and is quite unphysical. In CP-NaMo, saturation of the geometrically necessary dislocation density leads to a smooth transition towards lower work-hardening rate. Out of the two alloys considered, the predictions for the AA6060 alloy are the least accurate. The error is also not systematic for either of the two models.

The actual Taylor factor for the AA6082 alloy is quite close to the one for the random texture, and, thus, the difference between the stress-strain curves predicted by NaMo and CP-NaMo is less pronounced. However, the evolution of the Taylor factor is more noticeable than for the AA6060 alloy, which leads to better predictions of the work-hardening rate at large strains with CP-NaMo than NaMo. The predictions for the O temper fail again, but for the other tempers the predictions are fairly accurate. The initial yield stress deviates from the experimental one for tempers T6x and T7, but the predictions of the work-hardening are reasonably good for all tempers except the O temper.

The AA6060 in temper T4 alloy was used to evaluate how CP-NaMo describes the plastic anisotropy of the material. The anisotropy of the plastic flow is represented by ε_x versus ε_z diagrams in Figure 7, where ε_x is the logarithmic strain in the transverse direction of the specimen and ε_z is the logarithmic strain in the thickness direction of the extruded plate. The slope of the ε_x versus ε_z curve represents the strain ratio $r_y = d\varepsilon_x / d\varepsilon_z$, which would be unity for isotropic materials. As CP-NaMo could not predict the equivalent stress-strain curve accurately enough, the anisotropy of the flow stress is characterized by the flow stress ratio $\sigma_\theta / \sigma_{90}$ in Figure 8, where σ_θ is the flow stress in the actual tensile direction, denoted θ, and σ_{90} is the flow stress at $\theta = 90^\circ$ (i.e., in the transverse direction of the extruded profile) for the same amount of specific plastic work.

The plastic strain ratio r_y differs considerably between the specimens with different orientations and also evolves markedly in the course of plastic deformation. CP-NaMo reproduces the experimental results in a qualitative sense, both with respect to the initial value and the evolution of the strain ratio. In quantitative terms, the predictions are not accurate, especially for the 22.5° and 45° orientations. The experimental flow stress ratio $\sigma_\theta / \sigma_{90}$ evolves considerably as well. At specific plastic work corresponding to 5% equivalent plastic strain in the 90° direction, there is a global maximum at the 0° orientation and a local maximum at 67.5°. In the simulations, a local maximum occurs at the 0° orientation, while the global maximum is found at the 67.5° orientation. As the deformation progresses, a global maximum arises at the 45° orientation in both the experiment and the simulation. The large value of the flow stress ratio in the 0° orientation for some extruded AA6xxx alloys, which the CP simulations do not reproduce was reported previously [51]. To prevent this inconsistency from skewing the results for all the orientations, 90° orientation was used for normalization.

Another way to display the influence of texture evolution on the plastic anisotropy in uniaxial tension is to calculate the Taylor factor M as a function of plastic straining in the different material directions. The results are plotted in Figure 9. The importance of the evolution of the Taylor factor clearly depends on the initial texture of the alloy. The evolution of M is not significant for the AA6060 alloy in the 0° orientation, and as a result the assumption of a constant Taylor factor in NaMo should work reasonably well. But for less stable textures, especially the 45° orientation, the evolution is considerable and cannot be neglected in simulations. On the contrary, the evolution of M is less direction dependent but still significant in the simulations of the AA6082 alloy.

6. Discussion and conclusions

CP-NaMo provided some improvements over the baseline NaMo with respect to predicting the stress-strain curves of the two studied alloys in the reference direction, mainly by accounting for the texture influence in a better way than by using a constant Taylor factor. However, overall it did not improve the results, which are still dominated by the precipitation model. This model may be enhanced by including some other possible dislocation obstacles. For example, the Cr dispersoids that are present in the AA6082 alloy may be added as another sort of non-shearable particles. In this alloy, the yield strength was underestimated for all but

the T7 temper, unlike the AA6060 alloy where the stress was either overestimated or underestimated without a preference.

The precipitation model provides input for both the yield stress and the work-hardening model, and is therefore crucial for the accuracy of the predictions of the resulting stress-strain curves. Accordingly, inaccurate predictions of the precipitate structure will inevitably lead to deviations between the predicted and measured initial yield strength as well as work-hardening. There are a number of simplified assumptions both for the nucleation and the growth and dissolution equations which may be violated and cause errors in the predictions.

Inaccurate predictions by the precipitation model is probably a major reason for the deviations between predictions and measurements for the O temper, since this particular heat treatment has not been comprehensively investigated and verified for NaMo previously. For the O temper, the precipitation model predicts almost no formation of particles for the AA6060 alloy. This is an unrealistic result. There will be precipitation of coarse particles taking place during ageing at 350^{o}C [52], which is not captured by the nucleation law. A more accurate description of the nucleation would have changed the complete stress-strain curve through the introduction of coarse non-shearable Orowan particles and a corresponding increase in the density of geometrically necessary dislocations as well as an associated lowering of the solid solution level, leading to increased dynamic recovery and a decreased density of statistically stored dislocations.

The precipitation model is also a main reason for the deviations between NaMo and measurements for the underaged T6x temper condition. This is a demanding ageing heat treatment to predict since the nucleation rate may be very low for a certain time period at the start of the ageing, known as the “incubation time”. Since the incubation time is not included in the nucleation laws of the precipitation model, NaMo may be somewhat inaccurate for the early stages of ageing. For the present materials, the low composition alloy AA6060 exhibits a distinct incubation period, where the macroscopic yield strength remains almost constant, and where NaMo overestimates the precipitation and the corresponding yield stress significantly. This is in contrast to the AA6082, which due to its higher alloy content, does not show a pronounced incubation period and for which NaMo tends to underestimate the initial yield stress (see Figure 6).

The crystal plasticity part of CP-NaMo managed to add the influence of the evolving texture to the baseline NaMo. Figure 9 shows the predicted evolving Taylor factor due to the

texture evolution under straining, while Figure 7 and Figure 8 confirm that the main features of the texture evolution were reproduced by the CP model. The predictions of the strain ratio could be improved by using a more advanced homogenisation method, namely modelling individual grains with one or several finite elements (CP-FEM). The results in [41] indicate that CP-FEM allows to obtain more quantitatively accurate prediction of the anisotropy in plastic flow. Concerning the flow stress ratio, the experimental results seem to show that the texture is not the only source of strength anisotropy for the AA6060 alloy. The flow stress ratio is very high for the 0° orientation at lower strains and not captured in the simulations, but at higher strains the ratio is predicted well by the texture-based crystal plasticity model. This may be explained by a higher initial slip resistance on some of the slip systems, stemming from a high initial dislocation density on some slip systems. In the course of deformation, the dislocations are produced on all active systems and gradually the initial densities stop playing a significant role in the crystal response (see also [41]).

With respect to the tensile tests in the reference direction, NaMo and CP-NaMo predicted the general trends in the response of the two alloys in different heat treatment conditions and in some cases the predictions were quite close to the experimental curves. One should remember that these results were obtained without any reference to the actual tensile tests performed on these specimens, just using the chemical composition, the thermal history and texture measurements. In a qualitative sense, CP-NaMo predicted the higher yield stress and lower work-hardening rates of the T6x, T6 and T7 tempers as well as the lower yield stress and the higher work-hardening rate of the T4 and O tempers. This indicates that while the precipitate model still has some problems, it manages to capture the physical mechanisms of the particle precipitation and may be improved in the future. The crystal plasticity model managed to predict the plastic anisotropy of the material and even its evolution reasonably well based only on the measured crystallographic texture. These results would be impossible to obtain using the assumption of a constant Taylor factor adopted in the original NaMo. In addition, the precipitate model provides the crystal plasticity model with microstructural information, which is very hard to obtain experimentally, such as the solid solution concentration and the characteristic precipitate size and distance. Therefore, the implementation of crystal plasticity in NaMo is not only physically correct, but simply inevitable, if one aims to use nanostructure modelling for alloys with a wide variety of crystallographic textures. Also, further development of NaMo and CP-NaMo will help to

better understand the plastic behaviour of aluminium alloys on the grain level and how this behaviour is influenced by crystallographic texture, solute content and precipitate particles.

References

[1] Myhr OR, Grong Ø, Pedersen KO. A Combined Precipitation, Yield Strength, and Work Hardening Model for Al-Mg-Si Alloys. Metall Mater Trans A 2010;41:2276-2289.

[2] Taylor GI, Elam CF. Bakerian lecture. the distortion of an aluminium crystal during a tensile test. P Roy Soc Lond A Mat 1923;102:643-667.

[3] Taylor G, Elam C. The plastic extension and fracture of aluminium crystals. P Roy Soc Lond A Mat 1925;108:28-51.

[4] Grytten F, Holmedal B, Hopperstad OS, Børvik T. Evaluation of identification methods for YLD2004-18p. Int J Plasticity 2008;24:2248-2277.

[5] Beradai C, Berveiller M, Lipinski P. Plasticity of metallic polycrystals under complex loading paths. Int J Plasticity 1987;3:143-162.

[6] Zattarin P, Lipinski P, Rosochowski A. Numerical study of the influence of microstructure on subsequent yield surfaces of polycrystalline materials. Int J Mech Sci 2004;46:1377-1398.

[7] Saai A, Dumoulin S, Hopperstad O. Influence of texture and grain shape on the yield surface in aluminium sheet material subjected to large deformations, AIP Conference Proceedings, 2011;1353:85.

[8] Barlat F. Crystallographic texture, anisotropic yield surfaces and forming limits of sheet metals. Mat Sci Eng 1987;91:55-72.

[9] Barlat F, Richmond O. Prediction of tricomponent plane stress yield surfaces and associated flow and failure behavior of strongly textured FCC polycrystalline sheets. Mat Sci Eng 1987;95:15-29.

[10] Choi S-H, Brem J, Barlat F, Oh K. Macroscopic anisotropy in AA5019A sheets. Acta Mater 2000;48:1853-1863.

[11] Taylor GI. The Mechanism of Plastic Deformation of Crystals. Part I. Theoretical. P Roy Soc Lond A Mat 1934;145:362-387.

[12] Orowan E. Mechanical strength properties and real structure of crystals. Zeitschrift für Physik 1934;89:327-343.

[13] Kocks U. Laws for work-hardening and low-temperature creep. J Eng Mater 1976;98:76.

[14] Mecking H, Kocks U. Kinetics of flow and strain-hardening. Acta Metall Mater 1981;29:1865-1875.

[15] Bouaziz O, Barbier D, Embury J, Badinier G. An extension of the Kocks–Mecking model of work hardening to include kinematic hardening and its application to solutes in ferrite. Philos Mag 2013;93:247-255.

[16] Acharya A, Beaudoin A. Grain-size effect in viscoplastic polycrystals at moderate strains. J Mech Phys Solids 2000;48:2213-2230.

[17] Li J, Soh A. Modeling of the plastic deformation of nanostructured materials with grain size gradient. Int J Plasticity 2012.

[18] Kuhlmann-Wilsdorf D. Theory of workhardening 1934-1984. Metall Trans 1985;16:2091-2108.

[19] Baik SC, Estrin Y, Kim HS, Hellmig RJ. Dislocation density-based modeling of deformation behavior of aluminium under equal channel angular pressing. Mat Sci Eng 2003;351:86-97.

[20] Thomas G. Observations of dislocations and precipitates in aluminium alloys. Philos Mag 1959;4:606-611.

[21] Byrne J, Fine M-E, Kelly A. Precipitate hardening in an aluminium-copper alloy. Philos Mag 1961;6:1119-1145.

[22] Russell KG, Ashby M. Slip in aluminum crystals containing strong, plate-like particles. Acta Metall Mater 1970;18:891-901.

[23] Ashby M. The deformation of plastically non-homogeneous materials. Philos Mag 1970;21:399-424.

[24] Estrin Y, Mecking H. A unified phenomenological description of work hardening and creep based on one-parameter models. Acta Metall Mater 1984;32:57-70.

[25] Estrin Y. Dislocation theory based constitutive modelling: foundations and applications. J Mater Process Tech 1998;80:33-39.

[26] Kim JH, Lee M-G, Kim D, Wagoner R. Micromechanics-based strain hardening model in consideration of dislocation-precipitate interactions. Met Mater Int 2011;17:291-300.

[27] Cheng L, Poole W, Embury J, Lloyd D. The influence of precipitation on the work-hardening behavior of the aluminum alloys AA6111 and AA7030. Metall Mater Trans A 2003;34:2473-2481.

[28] Roters F, Raabe D, Gottstein G. Work hardening in heterogeneous alloys—a microstructural approach based on three internal state variables. Acta Mater 2000;48:4181-4189.

[29] Teodosiu C, Raphanel JL. Finite element simulations of large elastoplastic deformations of multicrystals, Proceedings of the International Seminar MECAMAT91, 1991;153-168.

[30] Tabourot L, Fivel M, Rauch E. Generalised constitutive laws for fcc single crystals. Mat Sci Eng 1997;234:639-642.

[31] Cédat D, Fandeur O, Rey C, Raabe D. Polycrystal model of the mechanical behavior of a Mo–TiC 30 vol.% metal–ceramic composite using a three-dimensional microstructure map obtained by dual beam focused ion beam scanning electron microscopy. Acta Mater 2012;60:1623-1632.

[32] Shiekhelsouk M, Favier V, Inal K, Cherkaoui M. Modelling the behaviour of polycrystalline austenitic steel with twinning-induced plasticity effect. Int J Plasticity 2009;25:105-133.

[33] Cherkaoui M, Soulami A, Zeghloul A, Khaleel M. A phenomenological dislocation theory for martensitic transformation in ductile materials: From micro-to macroscopic description. Philos Mag 2008;88:3479-3512.

[34] Schouwenaars R. Some basic results in the mathematical analysis of dislocation storage and annihilation in stage II and stage III strain hardening. Philos Mag 2014;94:3120-3136.

[35] Simar A, Bréchet Y, De Meester B, Denquin A, Pardoen T. Microstructure, local and global mechanical properties of friction stir welds in aluminium alloy 6005A-T6. Mat Sci Eng 2008;486:85-95.

[36] Myhr OR, Grong Ø. Modelling of non-isothermal transformations in alloys containing a particle distribution. Acta Mater 2000;48:1605-1615.

[37] Myhr OR, Grong Ø, Andersen SJ. Modelling of the age hardening behaviour of Al–Mg–Si alloys. Acta Mater 2001;49:65-75.

[38] Myhr OR, Grong Ø, Fjaer HG, Marioara CD. Modelling of the microstructure and strength evolution in Al–Mg–Si alloys during multistage thermal processing. Acta Mater 2004;52:4997-5008.

[39] Anjabin N, Karimi Taheri A, Kim H. Crystal plasticity modeling of the effect of precipitate states on the work hardening and plastic anisotropy in an Al–Mg–Si alloy. Comp Mater Sci 2014;83:78-85.

[40] Khadyko M, Dumoulin S, Børvik T, Hopperstad O. An experimental-numerical method to determine the work-hardening of anisotropic ductile materials at large strains. Int J Mech Sci 2014;88:25-36.

[41] Khadyko M, Dumoulin S, Cailletaud G, Hopperstad O. Latent hardening and plastic anisotropy evolution in AA6060 aluminium alloy. Int J Plasticity 2016;76:51-74.

[42] Engler O, Randle V. Introduction to texture analysis: macrotexture, microtexture, and orientation mapping. CRC press, 2010.

[43] Bridgman P. The stress distribution at the neck of a tension specimen. T Am Soc Met 1944;32:553-574.

[44] Le Roy G, Embury J, Edwards G, Ashby M. A model of ductile fracture based on the nucleation and growth of voids. Acta Metall Mater 1981;29:1509-1522.

[45] Johnsen J, Holmen JK, Myhr OR, Hopperstad OS, Børvik T. A nano-scale material model applied in finite element analysis of aluminium plates under impact loading. Comp Mater Sci 2013;79:724-735.

[46] Friedel J, Vassamillet L. Dislocations. Pergamon Press Oxford, 1964.

[47] Deschamps A, Brechet Y. Influence of predeformation and ageing of an Al–Zn–Mg alloy—II. Modeling of precipitation kinetics and yield stress. Acta Mater 1998;47:293-305.

[48] Li S, Engler O, Van Houtte P. Plastic anisotropy and texture evolution during tensile testing of extruded aluminium profiles. Model Simul Mater Sc 2005;13:783-795.

[49] Grujicic M, Batchu S. Crystal plasticity analysis of earing in deep-drawn OFHC copper cups. J Mat Sci 2002;37:753-764.

[50] Stander N, Roux W, Goel T, Eggleston T, Craig K. LS-OPT user's manual. Livermore software technology corporation 2008.

[51] Dumoulin S, Engler O, Hopperstad O, Lademo O. Description of plastic anisotropy in AA6063-T6 using the crystal plasticity finite element method. Model Simul Mater Sc 2012;20:055008.

[52] Milkereit B, Wanderka N, Schick C, Kessler O. Continuous cooling precipitation diagrams of Al–Mg–Si alloys. Mat Sci Eng 2012;550:87-96.

Tables

Table 1: Chemical composition of the alloys, wt%

Alloy	Fe	Si	Mg	Mn	Cr	Cu	Zn	Ti
AA6060	0.193	0.422	0.468	0.015	0.000	0.002	0.005	0.008
AA6082	0.180	0.880	0.600	0.530	0.150	0.020	0.005	0.011

Table 2: Heat treatment of the alloys

Temper	Stage 1	Stage 2	Stage 3	Stage 4	Stage 5
T4	540°C in salt bath for 15 min	Water quenching	One week at room temperature	___	___
T6x	540°C in salt bath for 15 min	Water quenching	15 min at room temperature	185°C in oil bath for one hour	Air cooling
T6	540°C in salt bath for 15 min	Water quenching	15 min at room temperature	185°C in oil bath for five hours	Air cooling
T7	540°C in salt bath for 15 min	Water quenching	15 min at room temperature	185°C in oil bath for one week	Air cooling
O	540°C in salt bath for 15 min	Water quenching	15 min at room temperature	350°C in salt bath for twenty four hours	Air cooling

Table 3: Parameters of crystal plasticity model

c_{11}, MPa	c_{12}, MPa	c_{44}, MPa	$\dot{\gamma}_0$, s^{-1}	m	$q_{\alpha\beta}$	μ, MPa	α	b, mm
106430	60350	28210	0.010	0.005	1.4, if $\alpha \neq \beta$ 1.0, if $\alpha = \beta$	24400	0.3	$2.86 \cdot 10^{-7}$

Table 4: Output of the precipitation and yield strength models of NaMo

Alloy/temper	$\hat{C}_{Mg}$, wt%	$\lambda_{g,o}$, m	f_o	τ_y, MPa
AA6060-T4	0.638	$1.00 \cdot 10^{9}$	$6.54 \cdot 10^{-22}$	17.6
AA6060-T6x	0.370	4.19	$6.55 \cdot 10^{-10}$	45.6
AA6060-T6	0.149	$2.52 \cdot 10^{-6}$	$1.11 \cdot 10^{-3}$	61.7
AA6060-T7	0.0450	$6.34 \cdot 10^{-7}$	$7.52 \cdot 10^{-3}$	44.9
AA6060-O	0.645	$4.40 \cdot 10^{3}$	0.00	12.7
AA6082-T4	0.882	$1.25 \cdot 10^{12}$	$6.54 \cdot 10^{-22}$	42.9
AA6082-T6x	0.511	$1.25 \cdot 10^{9}$	$1.04 \cdot 10^{-20}$	68.6
AA6082-T6	0.265	$1.55 \cdot 10^{-6}$	$1.82 \cdot 10^{-3}$	88.2
AA6082-T7	0.189	$4.63 \cdot 10^{-7}$	$9.71 \cdot 10^{-3}$	67.3
AA6082-O	0.288	$2.50 \cdot 10^{-5}$	$8.55 \cdot 10^{-3}$	22.7

Table 5: The parameters of CP-NaMo

Alloy/temper	k_2^{cp}	L, mm	ρ_g^{sat}, mm^{-2}
AA6060-T4	7.47	$4.72 \cdot 10^{13}$	$1.92 \cdot 10^{18}$
AA6060-T6x	11.68	$1.99 \cdot 10^{5}$	$4.49 \cdot 10^{7}$
AA6060-T6	24.59	$1.20 \cdot 10^{-1}$	$4.37 \cdot 10^{7}$
AA6060-T7	65.75	$3.01 \cdot 10^{-2}$	$2.58 \cdot 10^{7}$
AA6060-O	7.41	$2.09 \cdot 10^{8}$	$1.00 \cdot 10^{20}$
AA6082-T4	5.74	$5.91 \cdot 10^{16}$	$1.54 \cdot 10^{15}$
AA6082-T6x	8.98	$5.91 \cdot 10^{13}$	$9.47 \cdot 10^{9}$
AA6082-T6	15.36	$7.34 \cdot 10^{-2}$	$4.37 \cdot 10^{7}$
AA6082-T7	20.26	$2.20 \cdot 10^{-2}$	$2.74 \cdot 10^{7}$
AA6082-O	14.35	1.19	$5.77 \cdot 10^{5}$

Figures

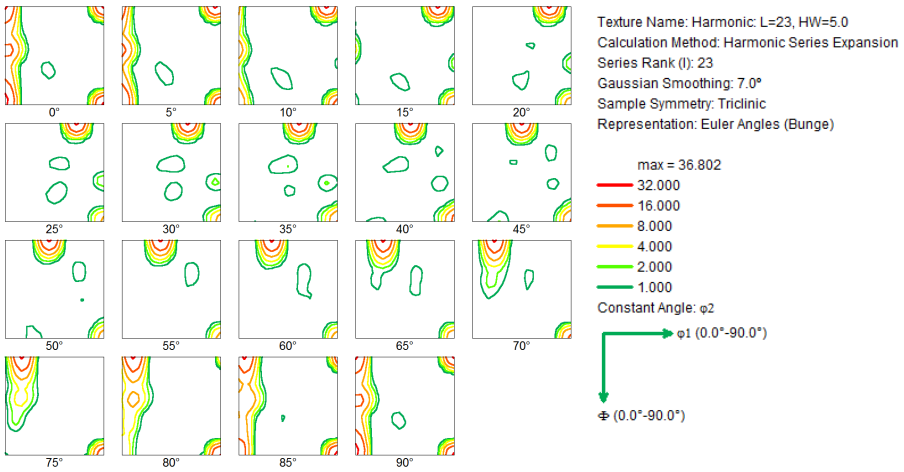

a)

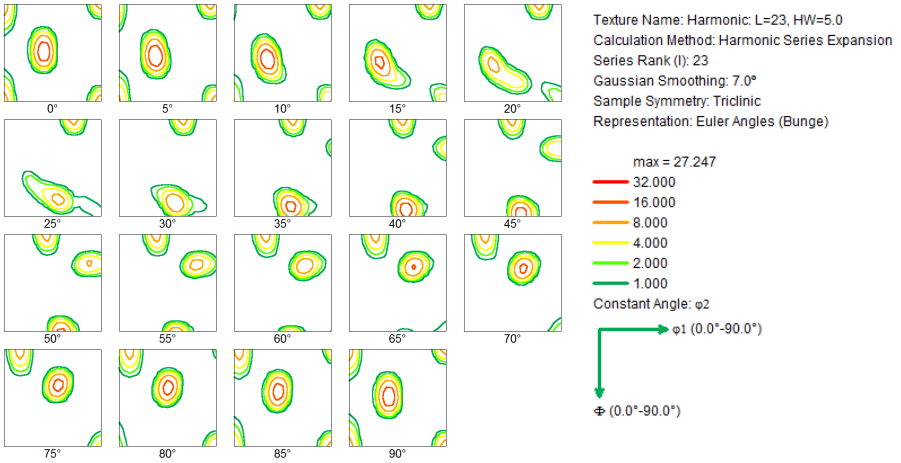

b)

Figure 1: Orientation distribution function (ODF) for the a) AA6060 and b) AA6082 alloys.

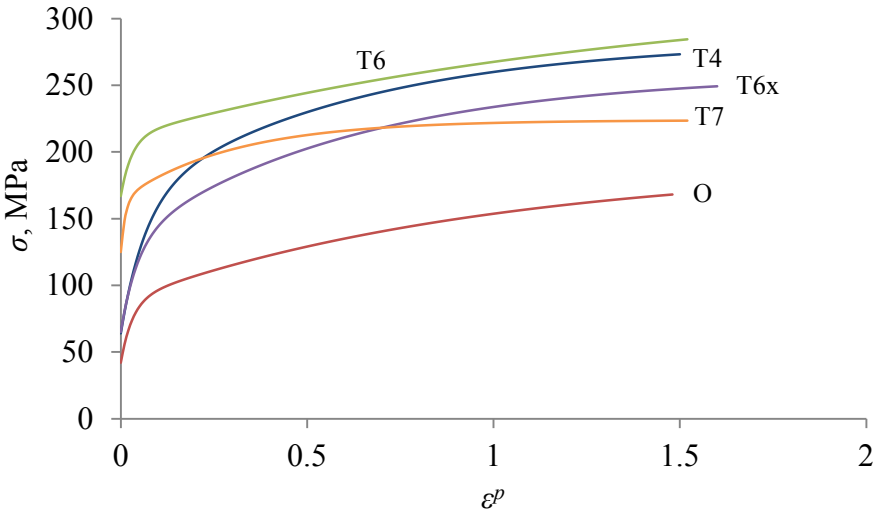

a)

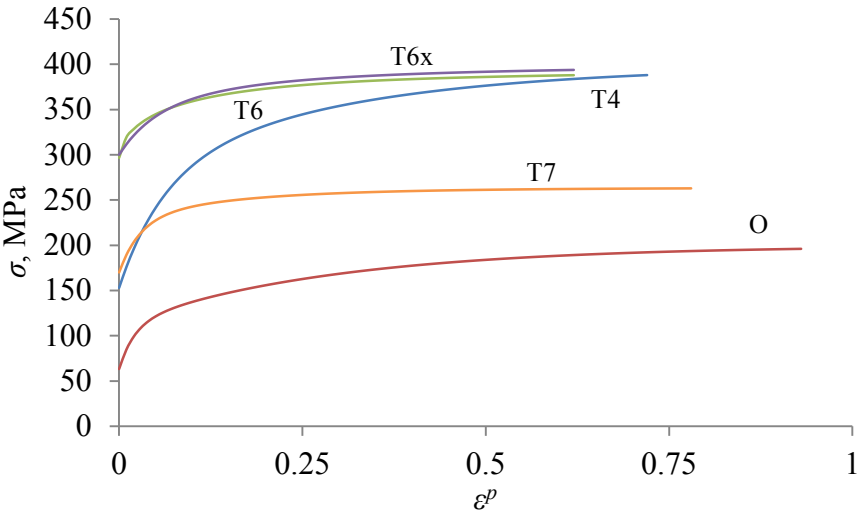

b)

Figure 2: Equivalent stress-strain curves for a) AA6060 and b) AA6082, using the extrusion direction as the reference direction [40].

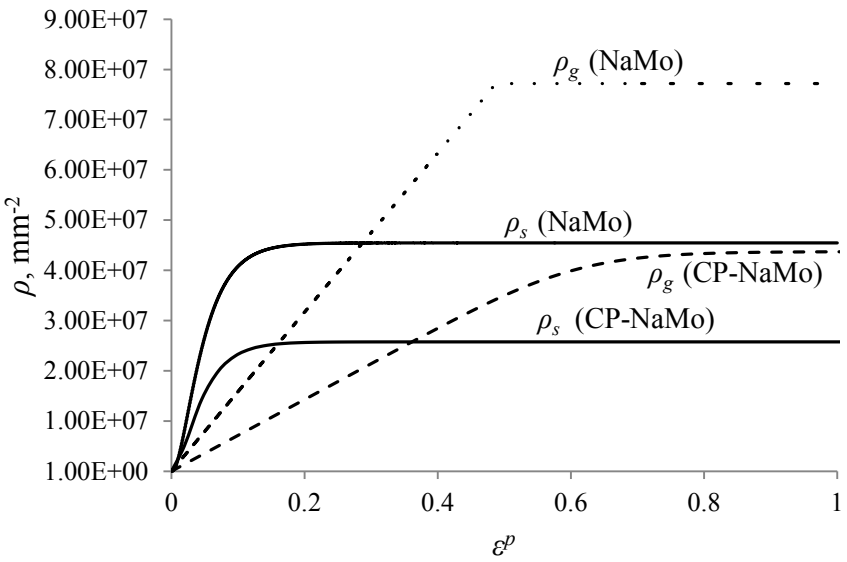

Figure 3: Dislocation density evolution in NaMo and CP-NaMo for AA6060-T6 material. The NaMo values correspond to average dislocation densities in the material, while the CP-NaMo values are taken from a simulation of a single crystal with a 100<001> (cube) orientation.

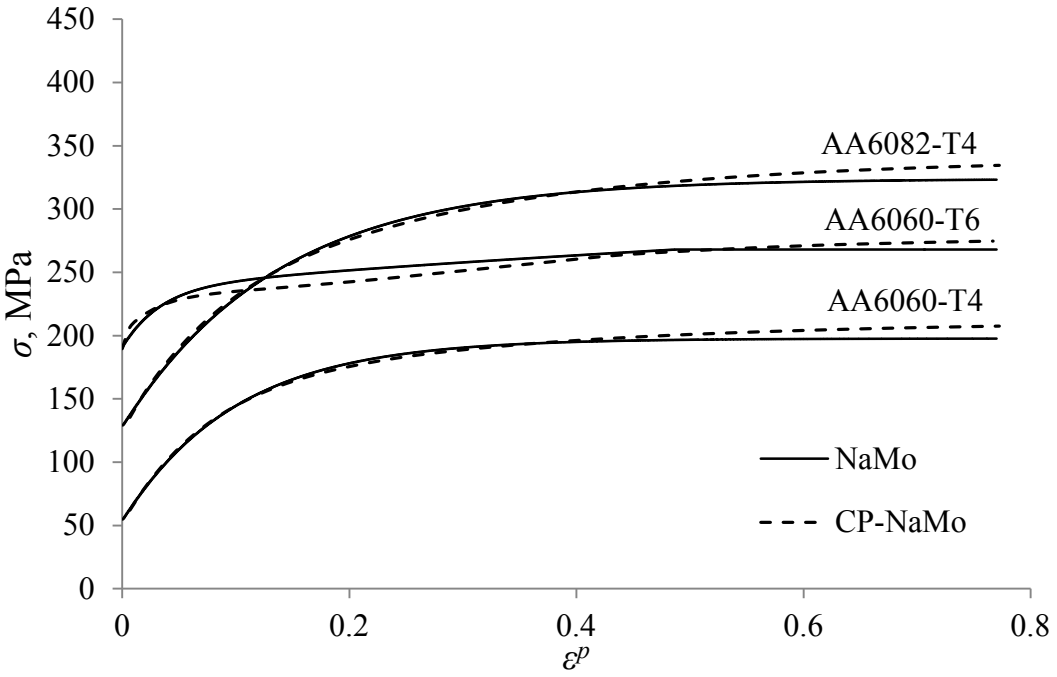

Figure 4: Equivalent stress-strain curves for AA6060 and AA 6082 alloys with random texture used in the calibration of CP-NaMo.

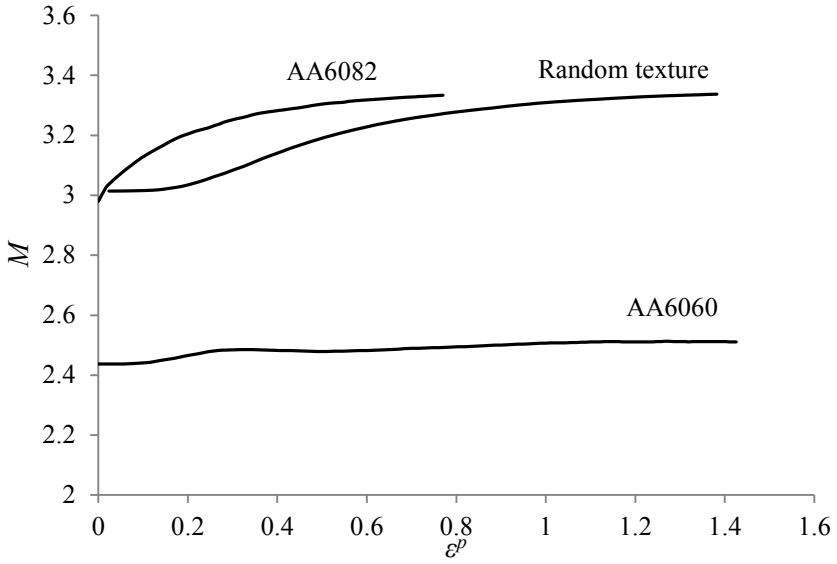

Figure 5: Evolution of the Taylor factor M with equivalent plastic strain ε^p in uniaxial tension in the reference direction simulated with the full-constraint Taylor model for the crystallographic textures of alloys AA6060 and AA6082 as well as random texture.

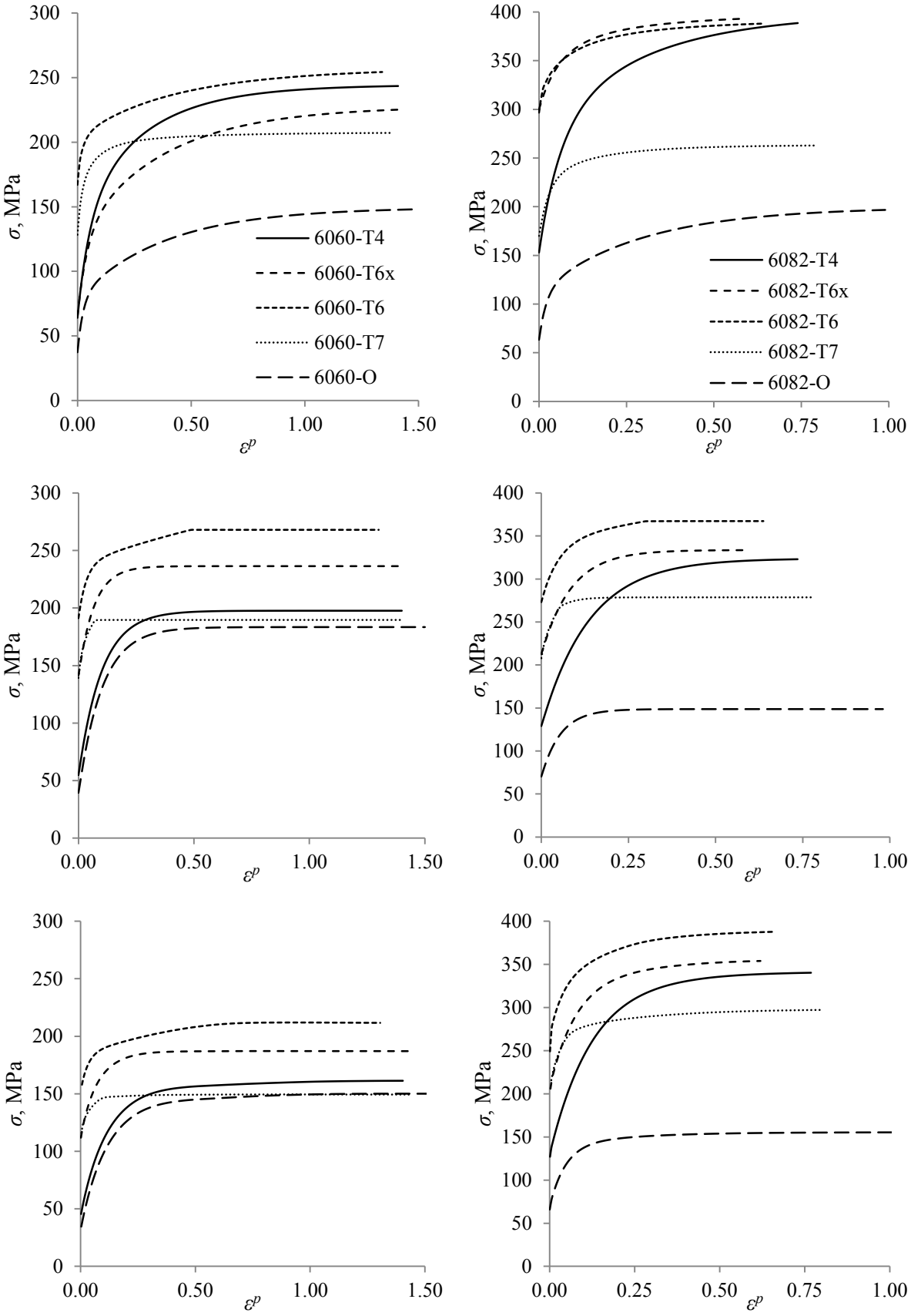

Figure 6: Comparison between experimental data (top), NaMo (middle) and CP-NaMo (bottom) for the AA6060 (left) and AA6082 (right) alloys in terms of the equivalent stress-strain curves in the reference (extrusion) direction.

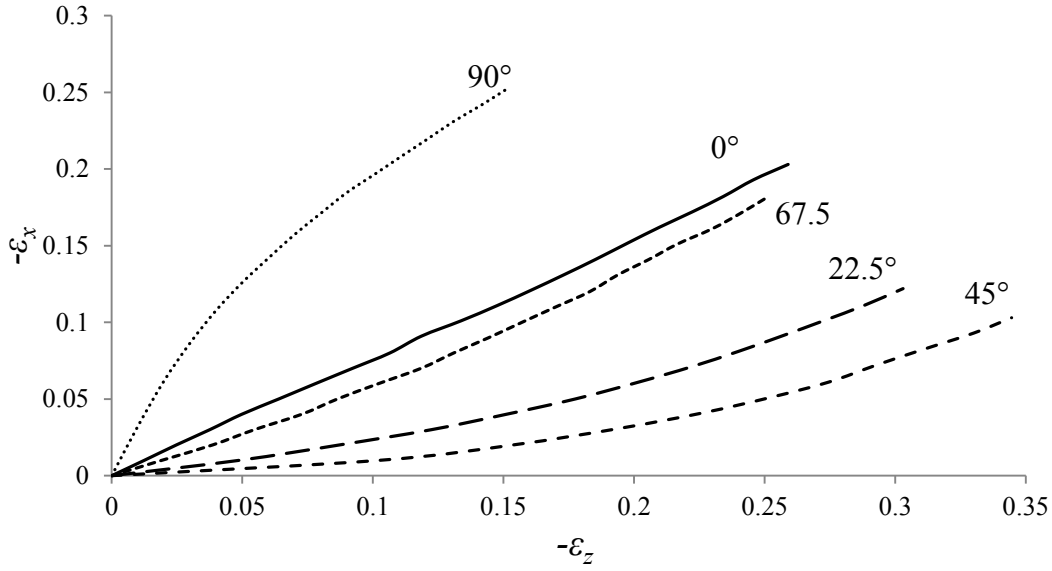

a)

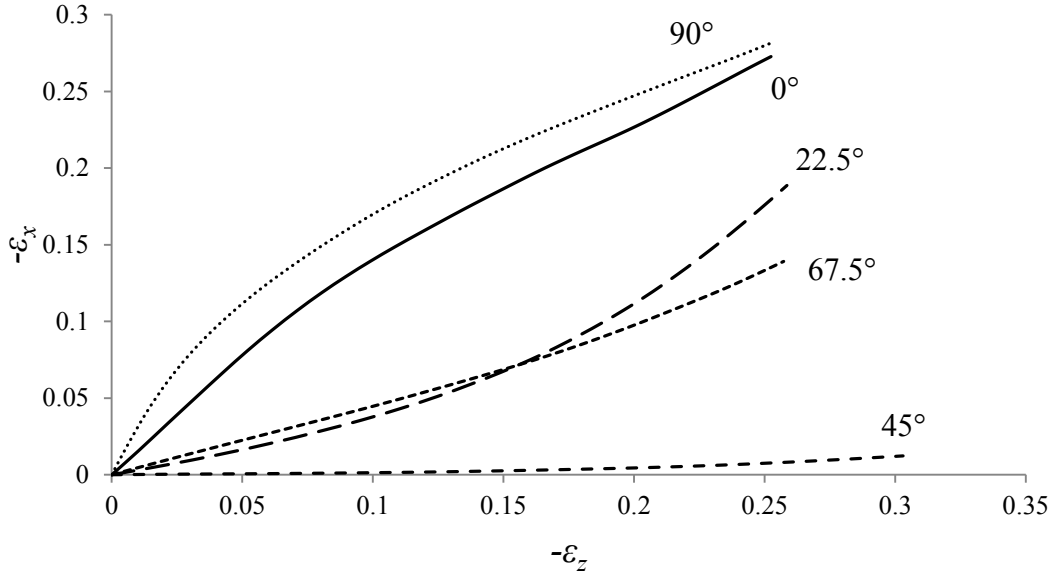

b)

Figure 7: Logarithmic width strain ε_x versus logarithmic thickness strain ε_z for the specimens in different directions for AA6060-T4 a) in experimental tests and b) in CP-NaMo simulations. The slope of these curves define the strain ratio $r_y = d\varepsilon_x / d\varepsilon_z$.

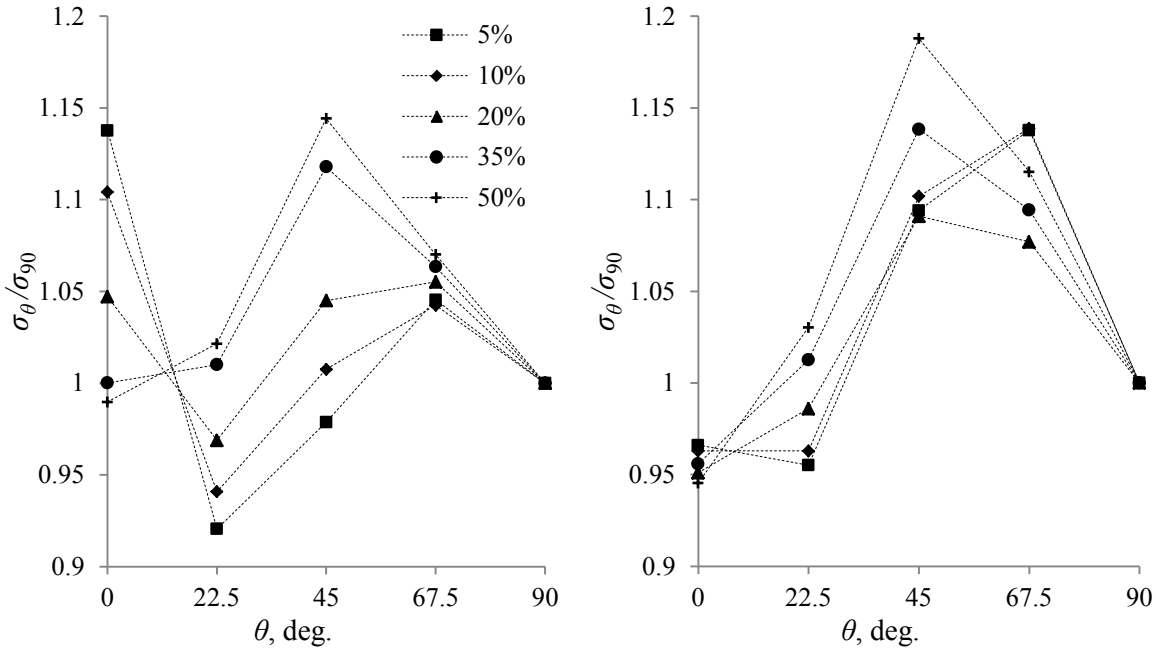

a) b)

Figure 8: Flow stress ratio $\sigma_\theta / \sigma_{90}$ for AA6060-T4 from a) experiment and b) CP-NaMo simulations versus specimen orientation θ. The flow stress ratio is taken at equal values of specific plastic work for all directions, corresponding to the plastic strain in the 90° direction given in the legend.

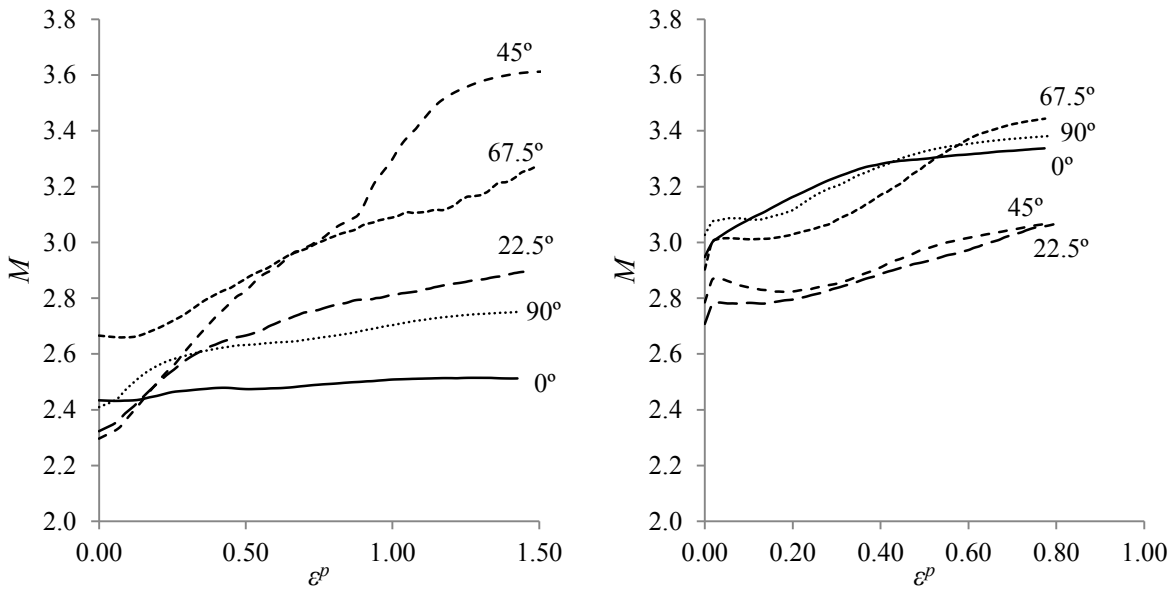

a) b)

Figure 9: Evolution of the Taylor factor M with plastic strain ε^p in uniaxial tension in different material directions simulated with the full-constraint Taylor model for the crystallographic textures of alloys a) AA6060-T4 and b) AA6082-T4.